A MODEL FOR ACTIVE REGION EMISSION AT CENTIMETER WAVELENGTHS

A. NINDOS
Section of of Astrophysics, Astronomy and Mechanics, Department of Physics, University of Athens, GR-15784 Athens, Greece

C. E. ALISSANDRAKIS
Section of Astrogeophysics, Department of Physics, University of Ioannina, GR-45110 Ioannina, Greece

G. B. GELFREIKH
Main Astronomical Observatory of the Russian Academy of Sciences, Pulkovo, 196140 St. Petersburg, Russia

M. R. KUNDU
Astronomy Department, University of Maryland, College Park MD 20742, U.S.A.

K. P. DERE
E. O. Hulburt Center for Space Research, U.S. Naval Research Laboratory, Washington, DC 20375-5000, U.S.A.

and

A. N. KORZHAVIN and V. M. BOGOD
St. Petersburg Branch of the Special Astrophysical Observatory of the Russian Academy of Sciences, Pulkovo, 196140 St. Petersburg, Russia

(Received 31 May, 1995; in revised form 25 October, 1995)

Abstract. We present multi-frequency observations and model computations of the microwave emission of a solar active region. The radio observations were obtained with the RATAN-600 at several wavelengths between 0.8 and 31.6 cm and with the VLA at 6 and 20 cm. The active region was also observed in the EUV O IV lines by the HRTS instrument aboard the Space Shuttle Spacelab-2 mission. These lines are formed in the chromosphere-corona transition region and their intensity ratio is sensitive to pressure. Photospheric magnetograms provided both the longitudinal and the transverse component of the magnetic field. The microwave observations were checked against model computations taking into account both the free-free and the gyro-resonance emission mechanisms and using the pressure data from the O IV lines. The magnetic field was computed through constant-α force-free extrapolations of the longitudinal photospheric field. We computed both the flux from 2 to 20 cm and the spatial structure of the microwave emission at 6 and 20 cm. The comparison of the computed and observed flux spectra allowed us to estimate the magnetic field strength at the base of the transition region and in the low corona, as well as the values of the conductive flux and the height of the base of the transition region. The model maps at 6 cm and 20 cm showed that α was not constant above the active region; the same conclusion was reached on the basis of the photospheric observations. The use of pressure measurements allowed us to identify microwave structures which were determined by pressure enhancements. At 6 cm the computations confirmed the fact that the magnetic field is the principal factor that determines the structure of sunspot-associated sources and showed that the effect of pressure variations was small. Pressure variations were more important at 20 cm, where the peak of the emission was associated with the sunspot and a diffuse component was associated with the plage which had an average pressure higher by a factor of 1.54 than the sunspot.

Solar Physics **166:** 55–87, 1996.

1. Introduction

High-resolution microwave observations of solar active regions have shown several types of sources which are associated with particular configurations of the magnetic field (i.e., sunspots, plages, coronal loops, and regions of transverse magnetic field).

The strongest component observed in the 2–6 cm range is associated with neutral lines of the photospheric magnetic field (Kundu and Alissandrakis, 1984; Alissandrakis *et al.*, 1992). These sources are associated with emerging flux and with high gradient of the longitudinal magnetic field and they are characterized by extremely steep flux spectra. A satisfactory model is lacking at the moment; however in some cases their observable quantities have been reproduced by gyrosynchrotron emission from a small population of mildly relativistic electrons (Alissandrakis *et al.*, 1993).

Sunspot-associated sources have been observed extensively around 6 cm, where their peak brightness temperature is a few million degrees (Kundu *et al.*, 1977). Their structure in total intensity (I) is fairly simple, with emission coming from an area about the size of the penumbra, sometimes with a depression above the umbra (Alissandrakis and Kundu, 1982). The circular polarization (V) structure is more complicated: the degree of circular polarization is higher at the edge of the I source; thus a 'ring' or 'horseshoe' structure is formed. Observations at different wavelengths sample different heights and physical conditions in the solar atmosphere, with longer wavelengths referring to higher levels. At wavelengths shorter than 6 cm the brightness temperature of sunspot associated sources decreases while at longer wavelengths (around 20 cm) their emission is obscured by the plage and/or coronal loop emission.

The properties of sunspot-associated sources have been interpreted in terms of the gyroresonance process with the relative importance of free-free emission increasing with wavelength. The structure of the source depends upon which of the low-order harmonics of the gyrofrequency are located in regions of high temperature, i.e. the transition region (TR) or low corona. Among the harmonics of the gyrofrequency, those higher than the fourth are optically thin and have no contribution to the emission. The fourth harmonic has some contribution to the extraordinary emission at long wavelengths (around 20 cm). At 6 cm, gyroresonance emission comes primarily from the 2nd and 3rd harmonic. Multifrequency observations of active regions allowed Gary and Hurford (1987) to observe the change in emission mechanism from gyroresonance to predominantly free-free at about 10 cm.

Model computations assuming a plane-parallel density and temperature structure of the atmosphere above the spot and either an extrapolation of the photospheric magnetic field (Alissandrakis, Kundu, and Lantos, 1980), or an axially-symmetric theoretical magnetic field model (Gelfreikh and Lubyshev, 1979; Krüger, Hildebrandt, and Fürstenberg, 1985) have confirmed the picture described above and have successfully reproduced the basic features of the observed I and V maps.

The assumption of a plane-parallel atmosphere is, however, only a first order approximation and sometimes deviations are significant (Alissandrakis and Kundu, 1982; White, Kundu, and Gopalswamy, 1991). In order to make further advances in model computations, one needs density (or pressure) measurements in the TR together with microwave observations. An opportunity for such coordinated observations arose in August 1985, when pressure measurements in the TR were available from the HRTS instrument aboard the Spacelab-2 mission. Simultaneous microwave observations were obtained with the VLA (6 and 20 cm) and the RATAN-600 (10 frequencies from 0.8 to 31.6 cm). In this work we present model computations of the microwave emission taking into account the pressure measurements as well as the photospheric magnetic field and we compare them with the radio observations in an effort to derive a self-consistent model of the active region under study.

2. Observations and Data Processing

Two active regions were present on the solar disk during our observing period. Active region NOAA 4680 was located in the northern hemisphere of the Sun and consisted of a prominent plage and a prominent filament; no sunspots were observed on August 2. Active region NOAA 4682 was located in the southern hemisphere; it consisted of an almost axially-symmetric preceding spot of negative magnetic polarity and had a well developed bipolar magnetic structure. The orientation of the dipole field of the region was highly inclined with respect to the east–west direction, being oriented almost north–south. Here we shall present observations and model computations for active region 4682 for August 2, 1985; this was the only region observed by HRTS and the only one of the two for which we had magnetograms.

2.1. RATAN-600 OBSERVATIONS

The active regions 4680 and 4682 were observed with the RATAN-600 radio telescope from July 30 to August 3, 1985. The RATAN-600 observations provided simultaneous one-dimensional fan beam scans of the Sun in I and V at eleven different position angles and at ten wavelengths: 0.8, 2, 2.3, 2.7, 3.2, 4., 8.2, 11.7, 20.7, and 31.6 cm. The observations started 1 hr and 20 min before the Sun's transit through the local meridian and ended 1 hour and 20 min after the transit. The resolution of the RATAN-600 (in the E–W and N–S directions) is given in Table I.

The two active regions were resolved in scans recorded in wavelengths shorter than 8.2 cm while from 0.8 to 2.3 cm the active region emission was nearly at the

TABLE I
Resolution of RATAN 1-dimensional scans

Wavelength	E–W resolution (arc sec)	N–S resolution (arc min)
0.8	7	5
2.0	17	13
2.3	19	15
2.7	23	18
3.2	27	21
4.0	34	26
8.2	72	53
11.7	96	76
20.7	180	134
31.6	264	205

same level as the quiet Sun. Consequently, scans at four wavelengths (2.7–8.2 cm) were available for further analysis.

From the original scans at the eleven position angles we computed two-dimensional maps. The first step in the data reduction was the correction of the position of each I scan with respect to the center of the disk. The absolute calibration was done by setting the flux of the Sun in each scan to the value published in *Solar Geophysical Data*. Before applying this correction we took into account the fact that at short wavelengths the RATAN north–south beam is narrower than the diameter of the Sun, so the beam cuts off a portion of the total flux of the Sun. We found that this missing flux is 49%, 35%, and 26% of the solar flux at 2.7, 3.2, and 4 cm, respectively. Subsequently, the V scans were corrected for polarization cross-talk from the I channel and were calibrated by using the calibration factors obtained for the I data. The V scans were furthermore shifted by the amount determined for the I scans of the same position angle in order to correct their position with respect to the center of the solar disk. The next step was the subtraction of the quiet-Sun background emission which was done in the manner described by Alissandrakis *et al.* (1993). In Figure 1 we present corrected R and L scans at 2.7, 3.2, 4, 8.2, and 20.7 cm.

After all corrections a dirty map was computed by combining the scans at different position angles. The last step was an attempt to free the dirty map of sidelobes, through the standard CLEAN method. The resolution of the August 2 clean maps was $0.5'$ by $6'$, $0.6'$ by $7.5'$, $0.7'$ by $8.7'$ and $1.4'$ by $14.3'$ at 2.7, 3.2, 4, and 8.2 cm, respectively. A detailed description of the processing of this data set is given by Nindos *et al.* (1996), where the full results are also presented. Here

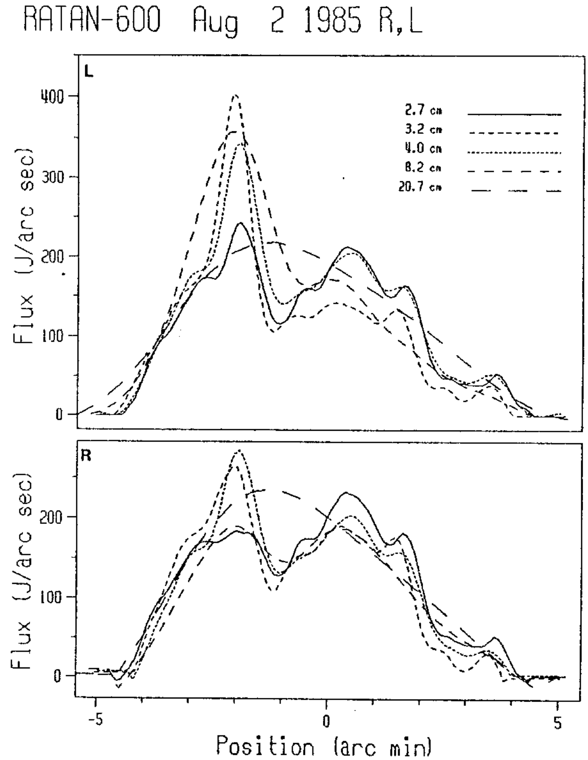

Fig. 1. Corrected one-dimensional scans of the active regions NOAA 4682 (peak at −2 arc min) and NOAA 4860 (peak at 0.5 arc min) obtained with the RATAN-600 in left (*top*) and right (*bottom*) circular polarization.

we shall only use flux density spectra for the sunspot associated source of active region 4682.

We used two methods for the measurement of the source flux from the RATAN maps. In the first method, the flux was estimated by visual determination of the local source limits and subsequent integration. In the second, the flux of each source was computed by modeling the maps with 2-dimensional gaussian-shaped sources. The two methods gave consistent results, within about 5%.

2.2. VLA OBSERVATIONS

The VLA observations were obtained from July 31 to August 3, 1985 at 6 and 20 cm. The observing procedure has been described by Alissandrakis, Kundu, and Shevgaonkar (1991). Approximately 7.5 hours of observations were used to produce synthesis maps in total intensity (I) and circular polarization (V) on August 2. The VLA was in the C-configuration, providing a spatial resolution of $4.3''$ by $4.1''$ at 6 cm and $17.4''$ by $16.8''$ at 20 cm.

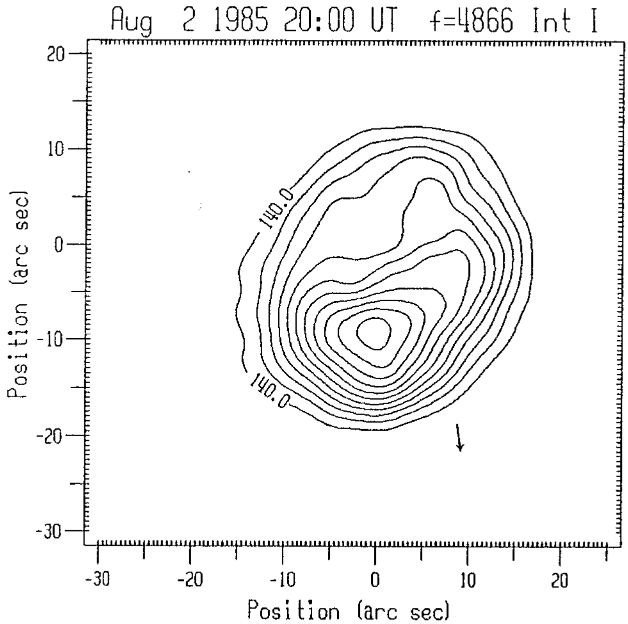

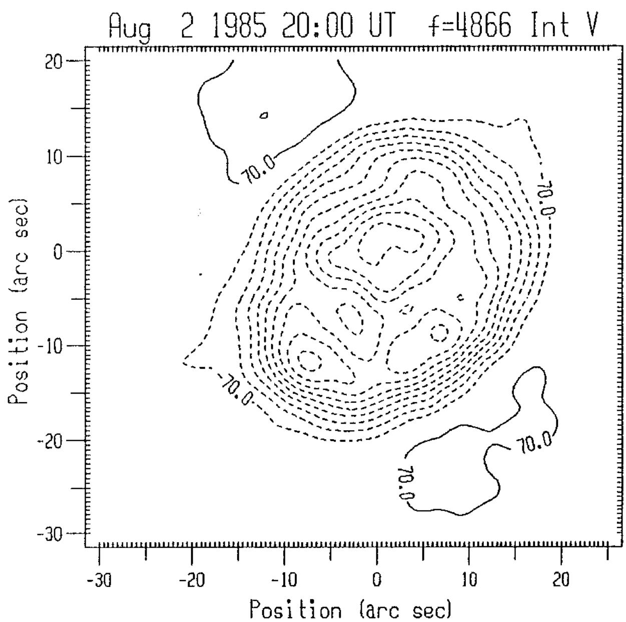

Fig. 2. Synthesized radio maps of active region 4862 observed with the VLA at 6.15 cm, in Stokes I, V and in L and R polarization. Contour levels are in brightness temperature steps of 1.4×10^5, 0.7×10^5, 10^5 and 1.5×10^5 K, respectively. Dashed contours denote negative values. The arrow shows the direction of the limb. In this and subsequent figures celestial north is up, celestial west to the right.

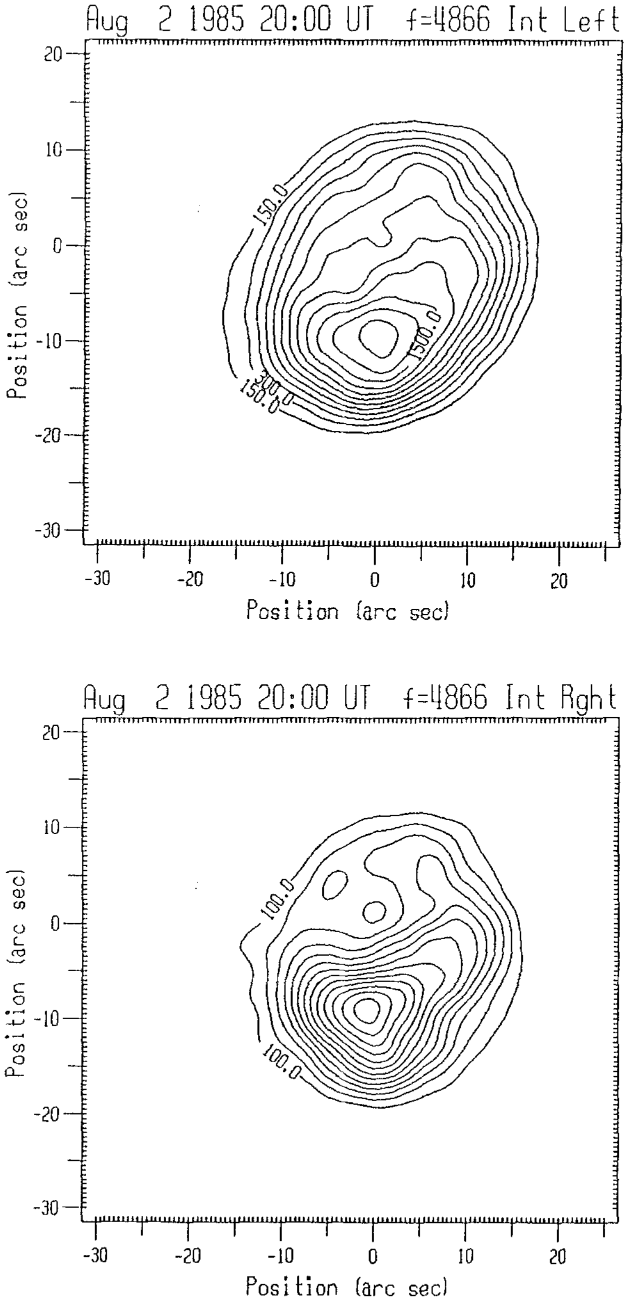

Fig. 2 (continued).

At the time of our observations, the flux calibration of the VLA was not reliable. We calibrated the VLA clean maps by setting their flux to the values derived from RATAN data. For the integration of VLA maps the lowest contour in the radio images which was regarded as reliable was at a level of about 10% of the peak

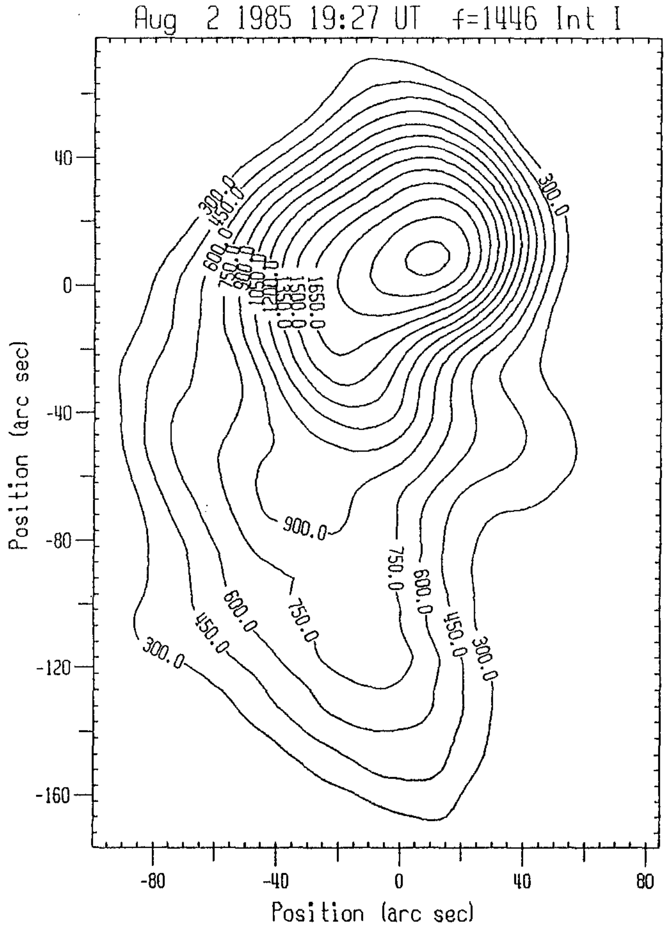

Fig. 3a.

intensity. There were no RATAN data available at 6 cm, we therefore interpolated between 4 cm and 8.2 cm. In Figure 2 we present the 6 cm VLA maps in I, V, L (left-hand circular polarization) and R (right-hand circular polarization). At 20 cm, the RATAN resolution was poor; the two active regions were not resolved and no maps were computed; thus we used the one-dimensional scans after background subtraction, in the manner described by Alissandrakis *et al.* (1993), to get the active region flux. Figure 3 shows VLA maps of NOAA 4682 at 20 cm in I, V, R, and L. We also applied the calibration procedure described above to the August 3 maps and our results were in good agreement with those of Kundu, Schmahl, and Fu (1989) who independently calibrated these maps. We should note that these calibration problems did not in any way affect the brightness distribution of the maps.

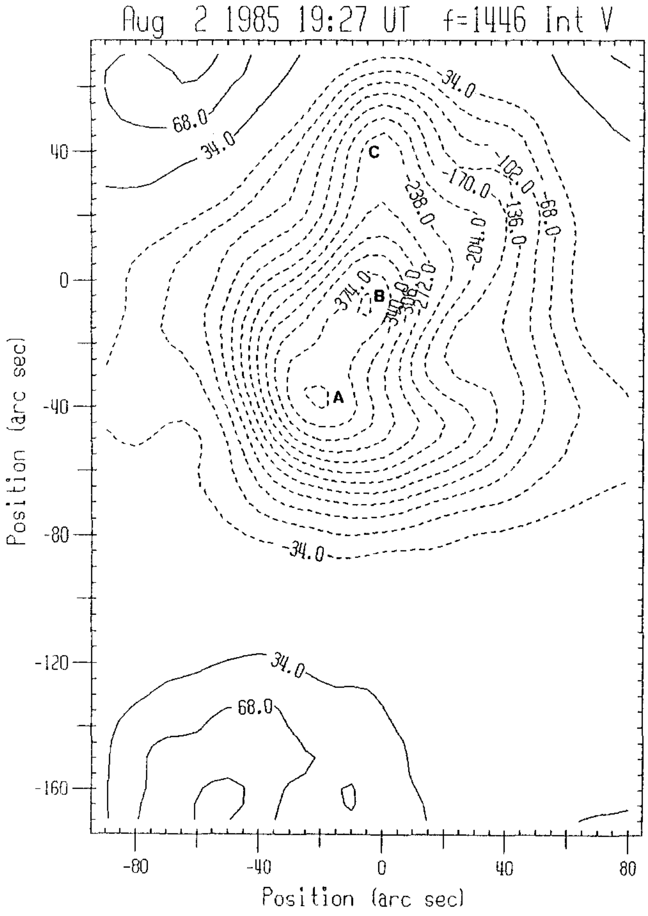

Fig. 3b.

2.3. HRTS OBSERVATIONS

Active region NOAA 4682 was observed in the EUV by the HRTS instrument aboard the Space Shuttle Spacelab-2 mission. Dere, Schmieder, and Alissandrakis (1990) described the observing procedure and analysed profiles of the C IV lines formed at 10^5 K in the chromosphere-corona transition region (TR). The HRTS mapped the active region 4682 on August 1, 1985 in the O IV lines (from 1399 to 1407 Å). The size of the maps was 980″ by 30″, with pixel spacings of 0.46″ by 3″. The O IV lines are formed in the TR at a temperature of 1.5×10^5 K and their intensity ratio is sensitive to pressure. We used the calculations of Dere, Bartoe, and Brueckner (1982) to derive the pressure from the O IV line ratios.

The O IV lines are intercombination lines with relative low A values and are not especially strong. Photographic film grain noise, enhanced by the high temperature encountered during the Spacelab-2 mission, can affect the deduced line intensities.

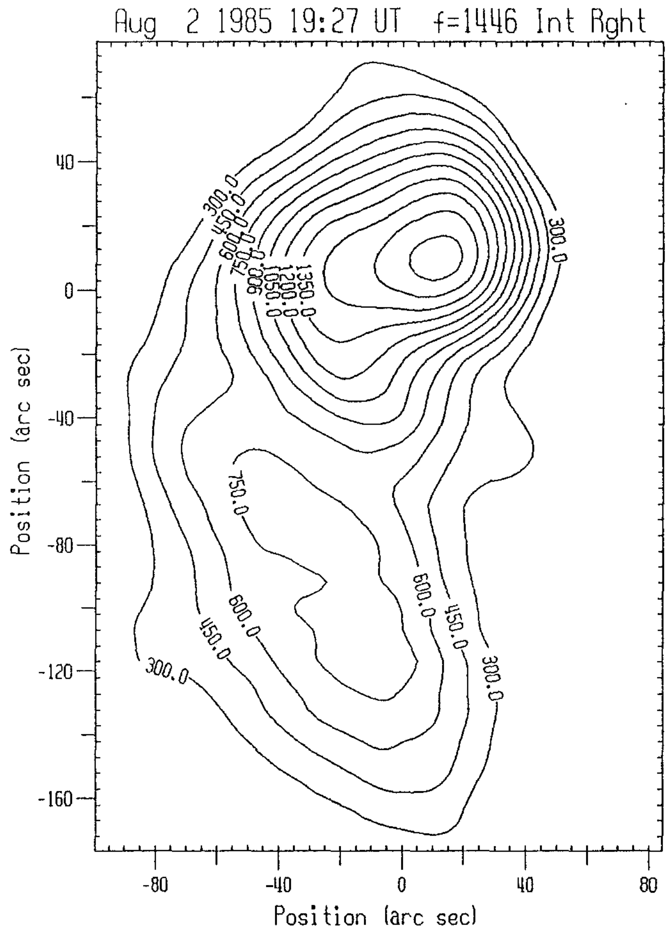

Fig. 3c.

Consequently some of the line intensities were observed to be outside the range predicted by the atomic model. A partial restoration was done by performing a second degree interpolation of deleted points by convolution of nearby data points which were not deleted. In order to reduce noise, we smoothed the pressure data by using a triangular filter in the direction of the spectrograph slit. These line intensities should reflect real variations in transition region pressures.

While sunspots are very well seen on the solar disk in photospheric and chromospheric emissions, they are practically indistinguishable in TR line intensities. However, Dere, Schmieder, and Alissandrakis (1990) had located the sunspot in C IV images. We computed the shift of the O IV image with respect to the C IV image by minimizing the sum of their absolute differences. The same technique was used for the computation of the shift of the O IV image with respect to Si I intensity images observed by HRTS. Both computations led to exactly the same results.

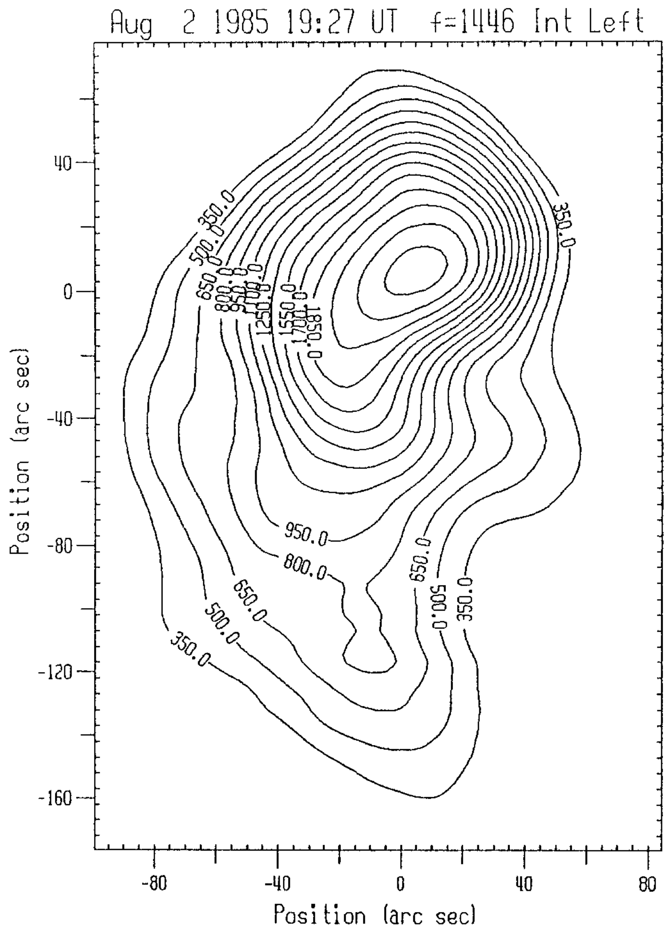

Fig 3d.

Fig. 3a–d. Same as Figure 2 for VLA 20.73 cm observations. Contour levels are in brightness temperature steps of 1.5×10^5 K for the I, R, and L maps and in 0.34×10^5 K for the V map.

Due to the lack of 6 cm VLA maps on August 1, we used the August 1 pressure data to create a pressure map for August 2, taking into account the solar rotation. Of course this computation is valid only under the assumption that no significant changes took place in the active region between August 1 and August 2. The study of Dere, Schmieder, and Alissandrakis (1990) verifies that this was the case. Figure 4 shows a gray-scale representation of the final pressure map, together with a contour plot of the longitudinal magnetic field from the Marshall Space Flight Center. The pressure data partly covers the spot and the plage.

Aug 2 1985 21:22 UT Int 170" x 225"

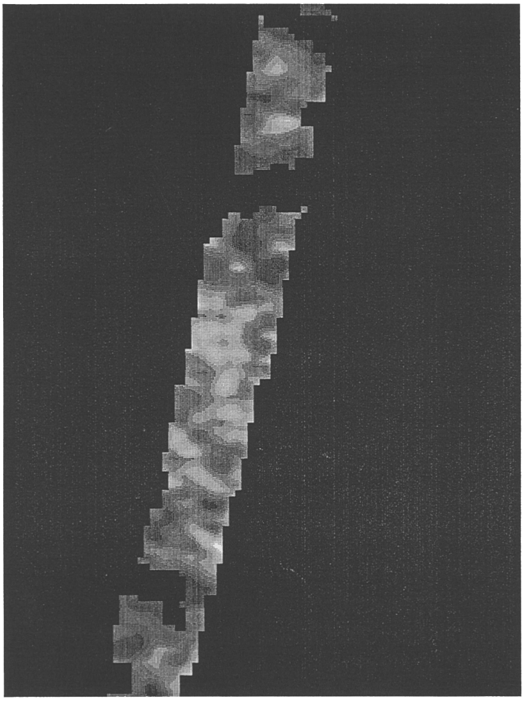

Fig. 4a.

2.4. Magnetic Field Observations

Photospheric magnetograms of active region 4682 were taken at Meudon and at the Marshall Space Flight Center (MSFC). The Meudon magnetogram provided the longitudinal (B_l) component of the field with pixel spacing $1.2''$ by $1.8''$ while MSFC provided both the longitudinal and the transverse component (its magnitude, B_t, and azimuth, ϕ) of the magnetic field vector with a pixel spacing of $2.8''$ in both directions.

The peak intensity of MSFC B_l data was 2340 G while the peak intensity of Meudon data was 1500 G. In order to better compare the two data sets, the Meudon longitudinal field was smoothed with a beam $10''$ by $10''$ and degraded to the resolution of MSFC field. Subsequently, we produced scatter plots between values of the two images and fitted the data to a second degree curve. We found that the Meudon magnetic field was lower than that of MSFC by a factor of 2 above the sunspot and by a factor of 1.5 above the plage. In order to make the two sets consistent we divided the MSFC field above the sunspot by $\sqrt{2} = 1.4$ and above the plage by $\sqrt{1.5} = 1.22$ and we multiplied the Meudon field by the same factor.

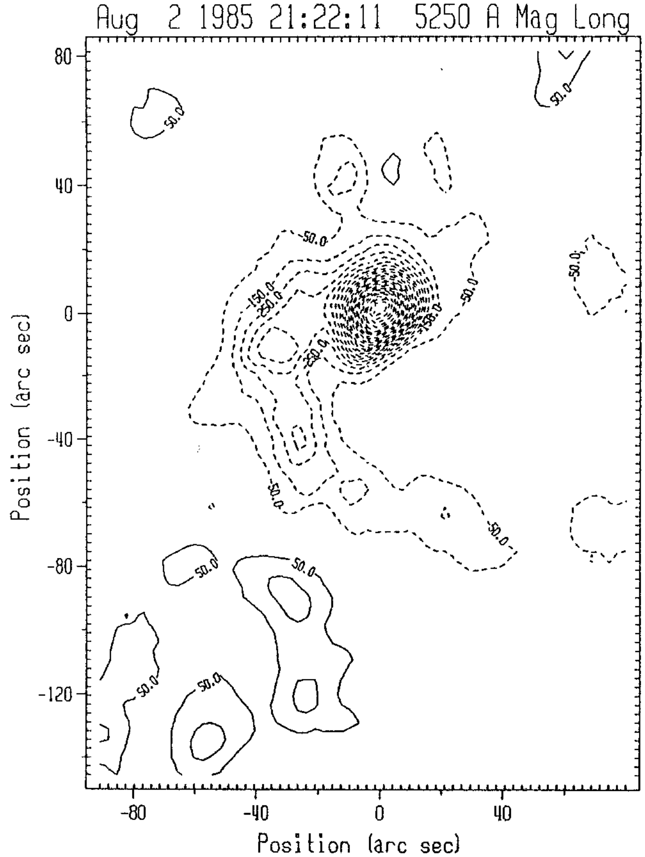

Fig 4b.

Fig. 4a–b. (a) Gray-scale representation of the pressure above the active region. (b) Contour plot of the longitudinal component of the magnetic field taken at MSFC. Dashed contours indicate negative polarity.

3. Model Computations and Results

The microwave emission in the extraordinary and ordinary modes was computed by integration of the transfer equation, taking into account thermal free-free and gyroresonance emission and absorption up to the fourth harmonic (for details see Alissandrakis, Kundu, and Lantos, 1980). The total intensity (Stokes parameter I) of the radiation is one half of the sum of extraordinary and ordinary brightness temperature, while the circular polarization (Stokes parameter V) in the quasi-longitudinal approximation used here (Zheleznyakov, 1970) is one half of their difference.

The computation requires knowledge of the electron temperature, the electron density and the magnetic field in the region of formation of radiation which is the TR and the low corona. The temperature structure in the region from 10^5 K up to the corona was determined by the assumption of constant conductive flux F_c, while at lower temperatures the model of Cheng and Moe (1977) was used; the corona was assumed to be isothermal with electron temperature $T_{\rm cor} = 3 \times 10^6$ K. The pressure was taken from the HRTS data; the O IV lines are formed at temperature of 1.5×10^5 K, from which we computed their height of formation under the constant conductive flux approximation (see Equation (13) of Alissandrakis, Kundu, and Lantos, 1980). The computation of pressure as a function of height was done under the assumption of hydrostatic equilibrium.

The east–west extent of HRTS images was not sufficient to cover the entire active region; thus for the points for which pressure measurements were not available we used the average value of the O IV map, which was 2.67×10^{15} cm^{-3} K. Thus, at least as far as the pressure is concerned, our models are not plane parallel; this is clearly an improvement over the previous models of active region radio emission.

The magnetic field was obtained from constant α, force-free extrapolations of the photospheric magnetic field from MSFC and Meudon. We computed the field up to a height of 3.2×10^4 km above the photosphere using the Fourier transform method developed by Alissandrakis (1981).

Our model is thus determined by three physical free parameters: the value of the conductive flux F_c, the height of the $T = 10^5$ K level, h_0 (which we shall call 'the base of transition region') and the value of α. In view of the discrepancy between the Meudon and MSFC photospheric magnetic field data we allowed for a fourth parameter, which was an overall correction factor for the magnetic field. The best possible model should reproduce the observed spatial characteristics of the VLA maps at 6 cm and 20 cm as well as the flux spectra derived from RATAN.

3.1. Flux Spectra

We computed model maps at 2.7, 3.2, 4, 6.2, 8.2, and 20.7 cm in extraordinary and ordinary mode; the quiet-Sun contribution was subtracted and the fluxes were obtained by subsequent integration. The VLA V map at 6 cm shows that the emission is polarized in the left sense, which corresponds to the negative magnetic polarity of the sunspot. At 20 cm the left sense of polarization extends over the neutral line to the region of opposite magnetic polarity and only a small part of that region is polarized in the right circular sense; this is apparently due to polarization inversion in the limbward part of the region, as a result of quasi-transverse wave propagation (Zheleznyakov, 1970). Thus for wavelengths of up to 8.2 cm, R and L polarization maps calculated from the observed I and V maps give the emission of the source in the ordinary and extraordinary mode respectively. However, this is not the case for the 20 cm, although the flux of the part of the V map which is not associated with negative magnetic polarity was around 10% of the total V flux.

The comparison of the observed and computed flux spectra allowed us to estimate the free parameters F_c and h_0 only, because the model flux values are practically independent of α. The best-fit values of F_c and h_0 were determined by using the chi-square criterion. We obtained $F_c = 6 \times 10^6$ erg cm^{-2} s^{-1} and $h_0 = 2000$ km.

In order to fit the observations with the model spectra we had to multiply the magnetic field by an extra factor of 1.3 at all levels. Taking into account the corrections we applied in order to reconcile the two data sets (see Section 2.4), as well as the effects of limited spatial resolution, this implies that the peak intensity of the longitudinal photospheric field reached 3000 G. This value seems to be quite high for a sunspot like the one we observed in NOAA 4682. However, according to *Solnechnye Dannye* (1985) the maximum photospheric field strength of that sunspot was around 2700 G which is close to our results. Without this correction the model maps would show no ordinary mode emission at 2.7 and 3.2 cm, contrary to the observations. Moreover, in order to reproduce the observed R and L flux densities for wavelengths longer than 3.2 cm, implausibly high values of F_c (around 10^8 erg cm^{-2} s^{-1}) would be required.

Figure 5 gives the observed flux spectra in R and L polarizations, together with the model spectra computed from MSFC magnetic field extrapolation for the best fit model as well as for two other models, one with one half and one with twice the conductive flux. Flux spectra computed using Meudon magnetic field extrapolations gave essentially the same results. The best-fit model flux spectra are consistent with the observed. The only problem appears in the 4 cm L data, which are not very reliable due to some instrumental problems in the 4 cm V channel. Note that there is a significant increase of the radio flux with F_c, so that our best fit value is good within a factor of less than two.

Let us now examine the flux spectra in more detail. From 2 cm to 2.6 cm there is little x-mode emission and no o-mode emission at all, in agreement with the RATAN observations where the active region emission was nearly at the same level as the quiet Sun. At 2.7 cm there is some o-mode emission and significant x-mode emission; the source is nearly 100% polarized. This shows that the third harmonic of the gyrofrequency is located in the low TR. The x-mode model flux increases in the range of 2 to 4.0 cm and reaches a maximum around 4 to 7 cm, whereas the o-mode flux increases in the range of 2.7 to 6.16 cm and reaches maximum around 8 cm. Up to $\sim$7 cm there is little gyroresonance emission from the plage because the magnetic field is not strong enough to produce optically thin emission at the third harmonic of the gyrofrequency. As the wavelength increases the plage emission increases and so does the emitting area. However, both the R and L flux decreased from 9 cm because both the second and the third harmonic are located in the upper part of the TR where the temperature gradient is small and cannot compensate the effect of the λ^2 factor.

This spectral behaviour shows that the third harmonic enters the TR at $\lambda \leq 2.7$ cm and reaches the upper part of the TR around 4.0 cm. The corresponding wavelengths for the second harmonic are around 3.2 cm and around 6.2 cm. Combining these results we get a lower limit of 1300 G and an upper limit of 1700 G for the strength

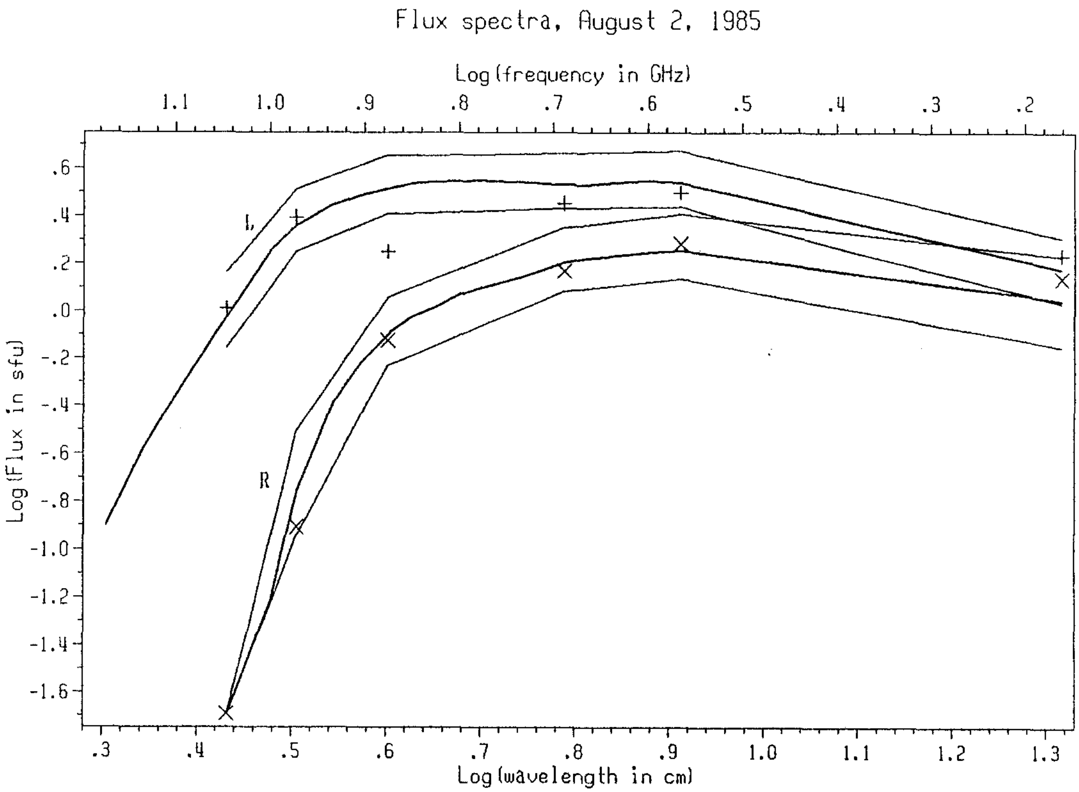

Fig. 5. Model flux spectra in R and L polarizations ($o-$ and x-mode, respectively) computed from MSFC magnetic field extrapolations for three cases: (i) $F_c = 6 \times 10^6$ erg cm^{-2} s^{-1}, $h_0 = 2000$ km, (thick lines), (ii) $F_c = 3 \times 10^6$ erg cm^{-2} s^{-1}, $h_0 = 2000$ km, (iii) $F_c = 1.2 \times 10^7$ erg cm^{-2} s^{-1}, $h_0 = 2000$ km. In the first case the flux was computed at wavelengths from 2 to 20.7 cm. In cases (ii) and (iii) the flux was computed for 2.7, 3.2, 4, 6.2, 8.2, and 20.7 cm. We also give the observed flux spectra in R ($\times$) and L ($+$).

of the magnetic field at the base of the TR. In the upper TR/low corona the lower limit is 500 G and the upper limit is 900 G.

3.2. 6 CM MODEL MAPS

The comparison between flux spectra derived from model computations and flux spectra derived from observational data allowed us to determine two of the three free parameters: the value of the conductive flux, F_c, and the height of the base of the TR, h_0. The third free parameter, the value of α, can be estimated from model computations at 6 cm and 20 cm and subsequent comparison between the model maps and the observed ones. The best-fit value should reproduce the basic spatial features of the VLA maps.

We used the Meudon magnetogram for the force-free extrapolations of the magnetic field because it provided better resolution than the MSFC magnetogram.

The magnetic field correction factors discussed in Sections 2.4 and 3.1 were taken into account. The computations were performed for the best fit values $F_c = 6 \times 10^6$ erg cm^{-2} s^{-1} and $h_0 = 2000$ km and the model maps were convolved with the VLA clean beam. For a given value of α, the model computations were performed twice. In the first model we did not take into account the spatial variation of the pressure but we simply did a plane-parallel computation, setting the pressure equal to the average value derived from O IV for the region above the sunspot (2.17×10^{15} cm^{-3} K). In the second model we took into account the spatial variation of pressure, thus relaxing the plane-parallel assumption. We should note that the observed R and L polarization maps can be compared directly with the extraordinary and ordinary mode model maps, respectively, because no propagation effects occurred above the spot (see Section 3.1).

Before discussing our results we would like to remind the reader of the factors that affect the structure of the 6 cm sources. The dominant contribution to the emission comes from the gyroresonance process. The structure of the sources depends upon which of the low-order harmonics are located in regions of high temperature. This, in turn, depends on the wavelength and the magnetic field. Once a given harmonic satisfies the above condition, the intensity of radiation is determined by its opacity which has much stronger dependence on the angle θ, between the magnetic field and the line of sight, than on any other physical parameter such as temperature and density. The opacity is zero at $\theta = 0$; thus there is always a region, around $\theta = 0$, where a given harmonic is optically thin. This region has considerable effects on the structure of the source: it shows up as a region of low intensity and it may produce ring or a crescent-shaped emission. A comparison of extraordinary and ordinary emission shows that the opacity of the medium is considerably greater in the x-mode; thus the circular polarization is low in regions where both harmonics are optically thick but it may go near the 100% level if the x-mode is optically thick and the o-mode is optically thin.

An inspection of the I, R, and L VLA maps (Figure 2) shows that the source is crescent-shaped (the crescent shows better in the I and R maps). The crescent is rather asymmetric with higher brightness temperatures towards the south side of the source. The I and R maps show a region of low intensity, which is associated with the zero-θ region; it is not located exactly above the center of the spot but shows a northward displacement. The peaks of the I, R, and L maps are not located in the direction of the limb but show a small clockwise rotation. These observable features can be interpreted in the frame of force-free magnetic fields with electric currents flowing parallel to the magnetic field. In the current-free case the field lines project radially on the photosphere, thus for a sunspot located at the center of the disk the 'zero-θ' region of low intensity is located at the center of the spot and the maximum intensity towards the limb (because the angle θ attains its highest values there). In the force-free case the twist of the field lines introduces a rotation of the radio source around the center of the spot; thus the maximum intensity is no longer located in the limbward direction.

The V map shows that the circular polarization is low at the locations of high total intensity. Maxima occur at three distinct regions: the first is associated with the zero-θ region and the others, located east and west of the I peak, in regions where only the third harmonic was located in the corona.

The best fit value of α should reproduce the observed structure of the VLA maps and should be consistent with the observed magnetic field configuration. We remind the reader that the constant α field is a simplification, but it is the only case that can be computed numerically from observational data. In the general case α is a function of position, with the only restriction being that it should remain constant along a field line.

In order to check the variation of α over the active region we compared the azimuth observed at MSFC with that computed from the longitudinal component of the field at zero height and for a constant value of α. Figure 6 shows the observed longitudinal component, the observed transverse component together with its azimuth, and the difference between the observed and computed azimuth, computed for $\alpha = 0$. The azimuth difference is negative (dashed contours) for $\alpha > 0$ and positive for $\alpha < 0$. These results indicate that there is a large region southwest of the spot consistent with $\alpha = 0$. There is, however, an extended region at the east and northeast side of the spot as well as a smaller region near the spot center (marked A in Figure 6(c)) consistent with positive α ($\sim 2 \times 10^{-5}$ km^{-1}); there is also a small region northwest of the spot (marked B in Figure 6(c)) consistent with negative α ($\sim -2 \times 10^{-5}$ km^{-1}). Finally, near the center of the spot, there are three small regions with large positive and negative azimuth difference which persist even for very large values of α. It is thus clear that α is not constant over the sunspot, being on the average positive. We note that Schmieder *et al.*, 1989 derived a value of $\alpha = 5.2 \times 10^{-6}$ km^{-1} for the same region, by comparing the azimuth of the transverse field with the orientation of chromospheric fine structures.

The basic characteristics of the R and L maps were best reproduced by $\alpha = 2.4 \times 10^{-5}$ km^{-1} for the L map and $\alpha = -2.4 \times 10^{-5}$ km^{-1} for the R map (see Figure 7 for the model maps and Figure 2 for the VLA observations). The fact that different values of α were required for each of the two modes apparently reflects the fact that α was not constant.

The computed R map shows quite well the low intensity region of zero-θ. The plane-parallel model and the non-plane parallel model gave very similar results and this indicates that the magnetic field is the dominant contributor to the emission. Indeed, in the O IV pressure map (shown in Figure 6(d)) there was a rather dense region (with peak pressure 5×10^{15} cm^{-3} K) located near the center of the spot, but a significant part of it was in the region of low intensity where the angle θ was small and the second harmonic was optically thin in the o-mode and remained so even for high values of density. The other dense regions were above weak fields and did not influence the radio emission. The asymmetry of both the observed and the model R crescent (i.e., higher brightness temperatures towards

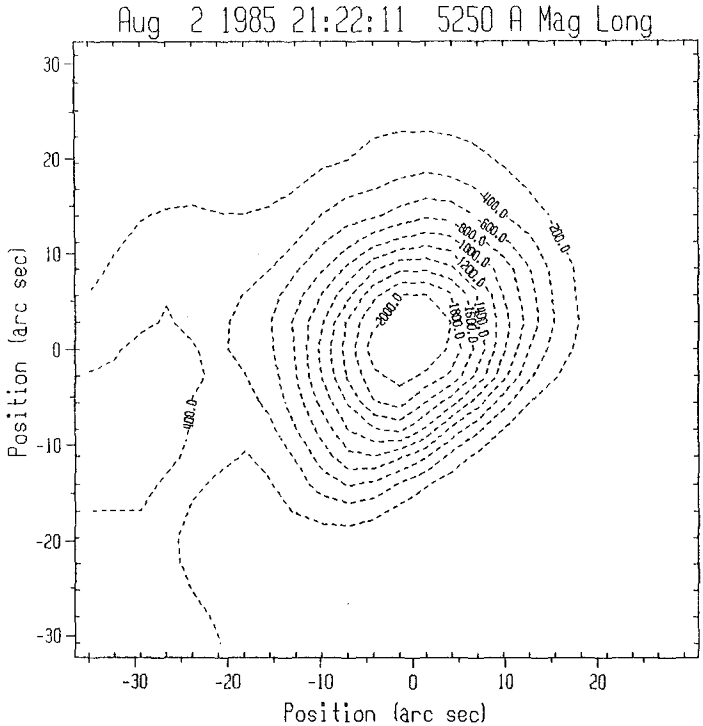

Fig. 6a.

the west) is due to the magnetic field strength: the Meudon magnetogram shows that the field is larger in the northwest direction than in the northeast direction. We would like to point out that model computations with positive values of α did not reproduce the above asymmetry and for these models considerable emission came not only from the west but also from the east side of the crescent. Using values of α lower than -2.4×10^{-5} km^{-1} we were able to suppress the east side of the crescent furthermore, but at the expense of a westward displacement of the peak R intensity.

In the computed L map the zero-θ region does not show well because of the higher opacity of the plasma to the extraordinary radiation. The VLA map shows higher brightness temperatures towards the northwest side of the source compared with the brightness temperatures towards the northeast side of the source. The plane-parallel, L, model cannot reproduce this asymmetry. However, maps computed using the real pressure values above the sunspot do show some asymmetry. This feature could therefore arise from pressure variations above the sunspot. An inspection of the O IV pressure map (Figure 6(d)) shows that there is a dense region (the one mentioned earlier, with peak pressure 5×10^{15} cm^{-3} K) in the region of higher T_b while at the location of relatively low T_b the average value of pressure was 1.58×10^{15} cm^{-3} K.

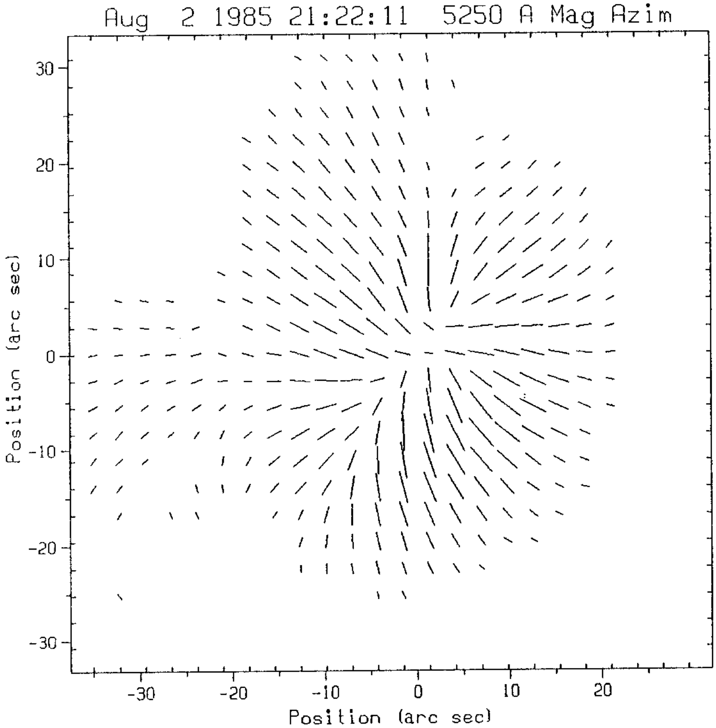

Fig. 6b.

The basic difference between the computed and the observed L maps is that the region of high T_b (above 1.5×10^6 K) is more extended in the model than in the observation. This implies that the model opacity there, is higher than the true. Almost the entire high T_b region was mapped by HRTS and the mean value of pressure was 1.62×10^{15} cm^{-3} K. This deviation could be interpreted in terms of the variation of the height of the base of the TR, which was assumed constant. Another possibility is that the constant conductive flux assumption was not valid above this region (see Chiuderi-Drago, Alissandrakis, and Hagyard, 1987). Finally, deviations of the magnetic field from the force-free model or even time variations in the interval between the magnetic field observations and the radio maps could result in an incorrect computation of the height of a given harmonic layer which, in turn, leads to incorrect calculation of the temperature of that layer.

Figure 8 shows model I and V maps computed from the R and L maps. The I map successfully reproduced the observed asymmetry of the crescent-shaped source, as well as the clockwise rotation of the maximum intensity with respect to the limb direction. The V map shows three maxima, in agreement with the observations; however the low polarization region is more extended than in the observed V map.

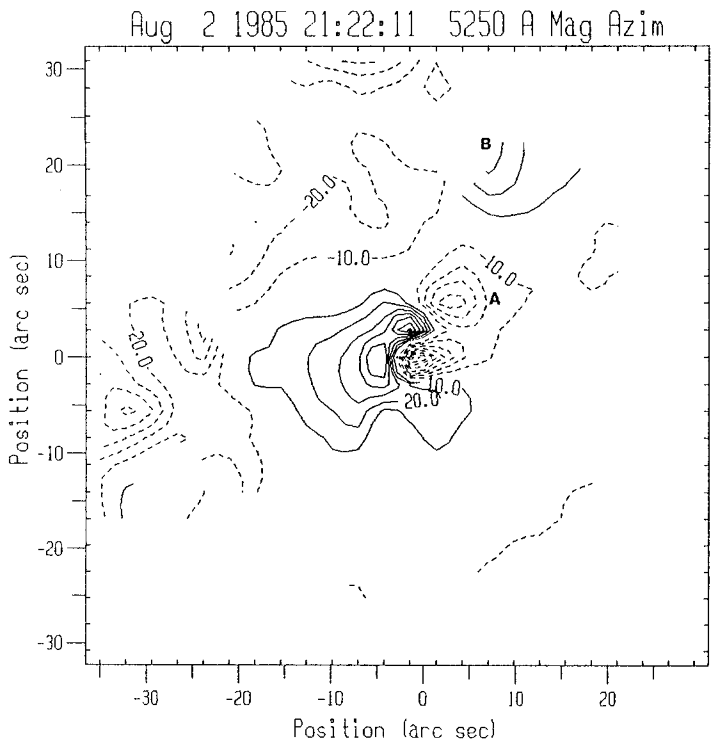

Fig. 6c.

3.3. 20 CM MAPS

The model computations at 20 cm were performed using the MSFC magnetic field observations, despite their lower resolution, because a 400 G region developed northeast of the spot between the time of the Meudon observation and the time of the MSFC observation. This new component of the magnetic field was responsible for the northeast component of the VLA V map (marked C in Figure 3). The magnetic field corrections discussed above were taken into account. Both plane-parallel and non-plane-parallel pressure models were computed (see Section 3.2 for details). In comparing the models with the observations one should keep in mind that the VLA R and L maps were affected by propagation effects; however this took place in a rather small part of the emitting area near the photospheric neutral line and did not seriously influence our study.

Both thermal gyroresonance (McConnell and Kundu, 1983; Shevgaonkar and Kundu, 1984) and thermal free-free (Lang, Wilson, and Rayrole, 1982; Dulk and Gary, 1983) mechanisms have been put forward to explain the 20 cm emission, while a large data set analysed by Gopalswamy, White, and Kundu (1991) was consistent with a free-free interpretation. Between 6 and 20 cm the free-free opacity increases, so that the dense plasma above the active region may become optically thick at 20 cm. In the same wavelength range the gyroresonance emission is rela-

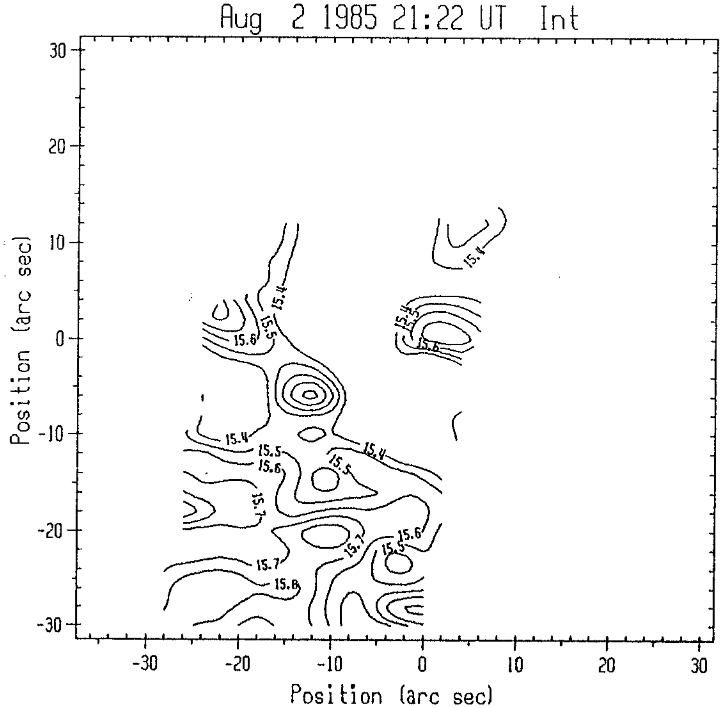

Fig 6d.

Fig. 6a–d. (a) Contour plot of the longitudinal component of the photospheric magnetic field in the sunspot region, from the MSFC observations. (b) The transverse photospheric field of the same region. The orientation of the segments indicate the azimuth of the transverse component; the length of the segments is proportional to the strength of the transverse component of the field. (c) Difference between the observed azimuth of the transverse field and the azimuth computed from the longitudinal component and for $\alpha = 0$. Contours labels are in degrees. (d) Contour plot of the pressure above the sunspot. Contour values are in logarithm of pressure (cm^{-3} K).

tively steady and thus the contrast between regions of large (sunspot) and moderate (plage) magnetic field decreases. Moreover, the circular polarization is lower at 20 cm. The part of the emission which is due to the free-free process is weakly polarized, while the brightness difference between the two modes of gyroresonance emission decreases; this is because of the increase of the *o*-mode opacity of the third harmonic and the decrease of the difference in electron temperature between the second and third harmonic layers, as they are located in higher regions of small temperature gradient.

The 20 cm emission came from a more extended region than the 6 cm emission and covered about the same area as the plage. It consisted of two components: a strong component associated with the sunspot and a diffuse component associated with the plage. The close similarity of the shape of the diffuse component with the underlying Hα plage (cf., Figures 4(b) and 3) and the fact that it showed no

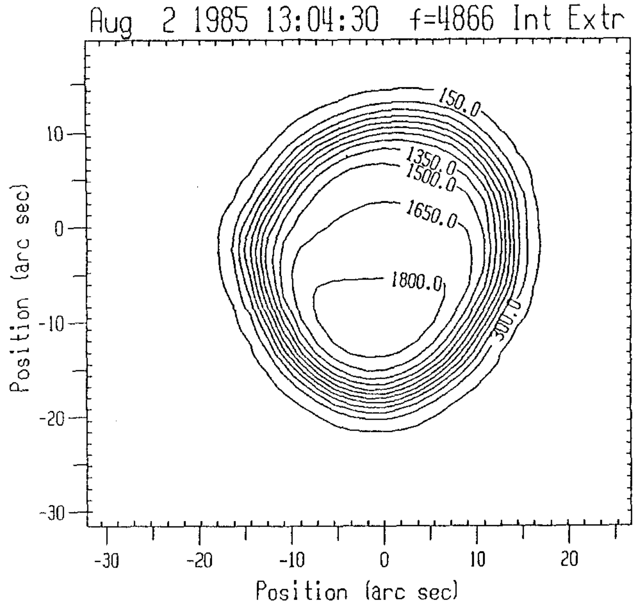

Fig. 7a

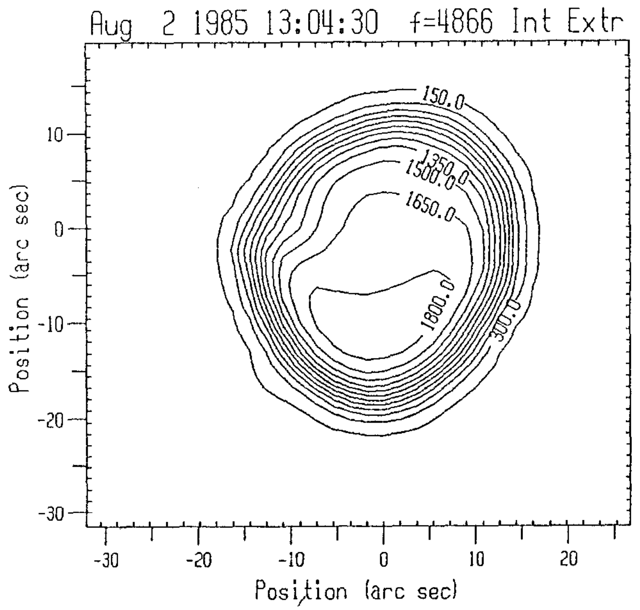

Fig. 7b.

changes due to perspective effects as the active region crossed the solar disk, led Alissandrakis, Kundu, and Shevgaonkar (1991) to attribute its origin primarily to plage emission. The similarity of the R and L maps implies that the circular polarization was low; indeed, the average degree of the circular polarization over the entire active region was 6% and around 20% at the location of the V peak. The last

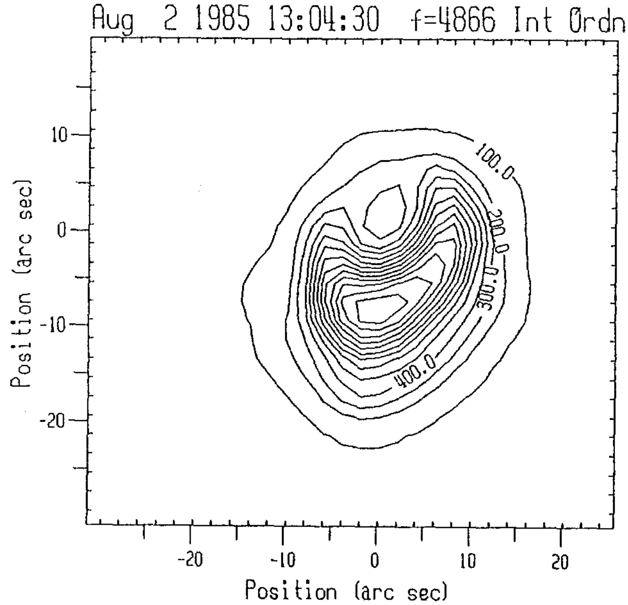

Fig. 7c

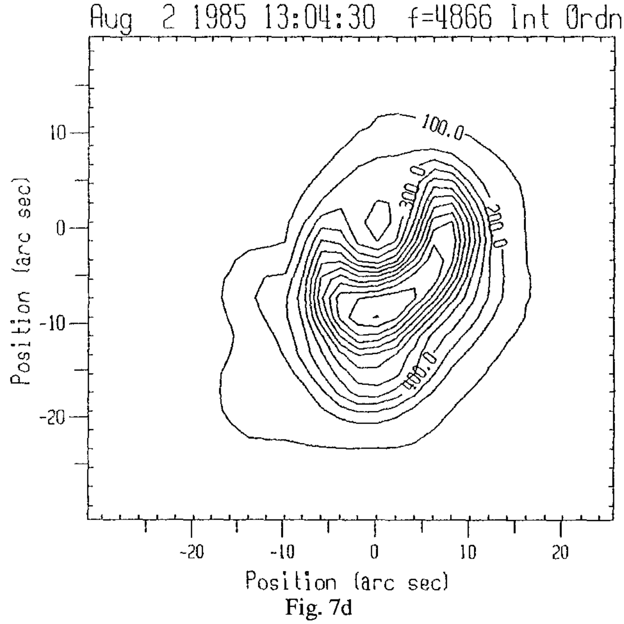

Fig. 7d

Fig. 7a–d. Model computations at 6 cm in R (a, b) and L (c, d) circular polarization. The R map was computed with $\alpha = -2.4 \times 10^{-5}$ km^{-1} and the L map with $\alpha = 2.4 \times 10^{-5}$ km^{-1}. Model computations were performed assuming a plane-parallel atmosphere (top) and by using O IV pressure values (bottom).

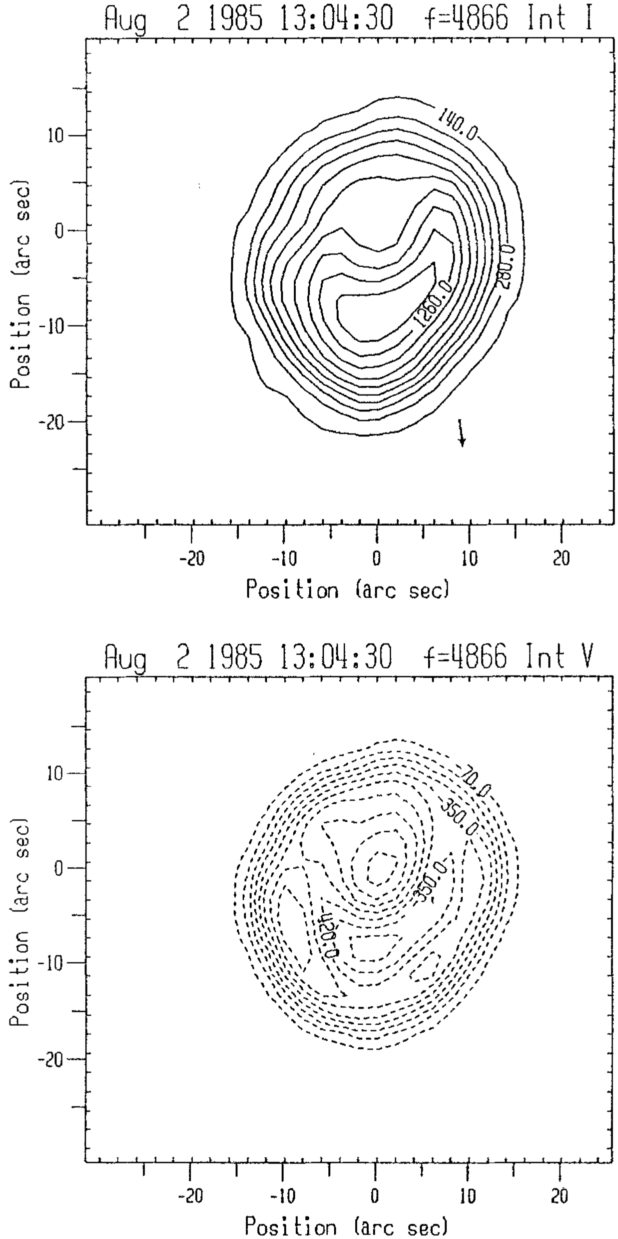

Fig. 8. Model I and V maps calculated from the R and L maps of Figure 7. The arrow shows the direction of the limb.

result is in good agreement with the statistical analysis performed by Gopalswamy, White, and Kundu (1991). The V map shows three peaks. The strongest (marked A in Figure 3) was located near the middle of the active region and was associated with the spur-shaped plage region. The second (B in Figure 3) was associated with the edge of the penumbra of the spot and the third (C in Figure 3), which lay northeast of the spot, was associated with the appearance of new magnetic flux (see above). We should also note that the circular polarization above the spot was low.

The limitations of the constant-α approximation were discussed in Section 3.2. At 20 cm, the emission comes from an extended region thus the situation is perplexed further. Among the various constant-α model maps, those with $\alpha = 0$ for both R and L best reproduced the basic characteristics of the observed V map, in particular the three peaks described above.

Model R and L maps computed with $\alpha = 0$, with and without the plane-parallel assumption, are presented in Figure 9; Figure 10 shows the computed I and V maps for the non-plane-parallel model. A comparison of the two model sets shows more pronounced differences than at 6 cm. The plane-parallel model cannot reproduce the observed spur-shaped emission from the plage, where the average pressure was 3.34×10^{15} cm^{-3} K (a factor of 1.25 higher than above the active region). However, the observed diffuse emission was more extended than shown by the model maps. This is probably due to emission from coronal loops, in particular near the photospheric neutral line towards the limb. Another difference is that the model R, L and I maxima are broader than the observed, probably due to the limited spatial resolution of the MSFC magnetogram.

In regions of strong magnetic field (sunspot) both the second and the third harmonics of the gyrofrequency are located in the low corona and thus are optically thick. Gyroresonance emission is not limited in the area above the spot, but extends over part of the plage; the third harmonic at 20 cm comes from the 170 G level, which is in the TR above the plage. Optically thin emission from the fourth harmonic at 20 cm requires a magnetic field strength of 130 G in the TR and sufficiently high angles between the magnetic field and the line of sight. The first harmonic requires a magnetic field strength of 510 G in the TR; however, the level of reflection at 20 cm occurs at $N_e = 2.6 \times 10^{10}$ cm^{-3}, which was not always below the TR according to the O IV pressure data. Taking into account the above constraints for the first harmonic, we found that it could radiate only above the sunspot where the pressure was low enough to bring the reflection layer below the base of the TR. However, the x-mode emission from the first harmonic was suppressed by the optically thick third harmonic emission, while the o-mode partly filled the hole of the zero-θ region. The zero-θ region was thus covered partly by free-free emission and partly by first harmonic emission. A consequence of the above is the fact that the peak intensity of the observed I, R, and L maps as well as the peak intensity of the model maps was associated with the sunspot.

The model V map shows three peaks (marked A, B, and C in Figure 10), in agreement with the observations. The strongest peak, A, was associated with the fourth harmonic, which produced optically thin x-mode emission and no o-mode emission. The underlying photospheric field strength was 550 G and its angle with the line of sight was 75°. The other two peaks of the V map were associated with regions where the x-mode emission from the third harmonic was optically thick

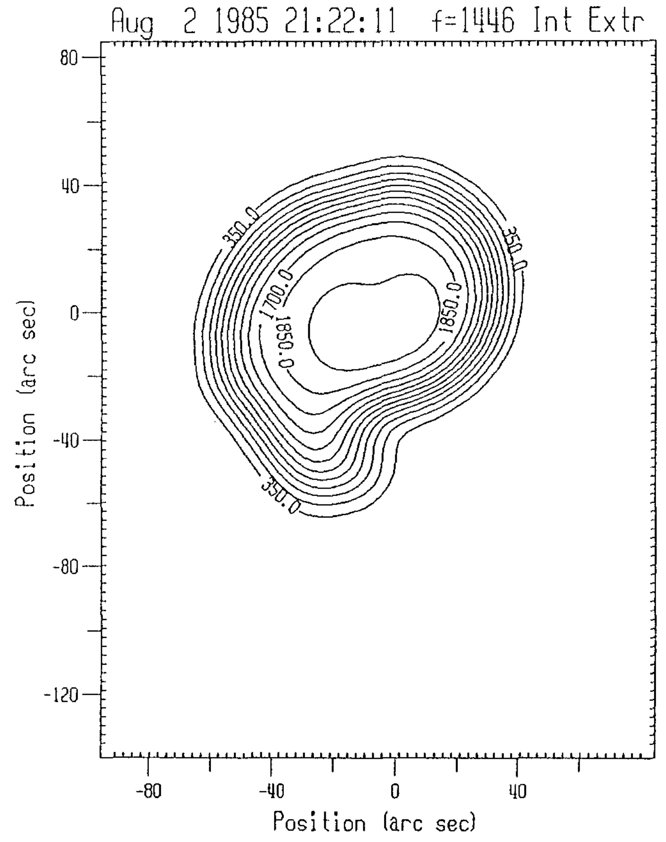

Fig. 9a.

while the optical depth of the *o*-mode emission from the second harmonic was low. The southern part of the model map is different from the observed because the latter was affected by propagation effects which have not been taken into account in our computation.

4. Summary and Conclusions

We presented multi-frequency observations and model computations of the microwave emission of a solar active region, taking into account not only the photospheric magnetic field but the pressure variations in the TR as well. Previous comparisons of models with observations treated the spatial structure at a single wavelength or used only flux data. This is also the first time that the pressure is derived directly from observations.

We performed detailed model computations of both the flux from 2 to 20 cm and the spatial structure of the emission at two wavelengths (6 and 20 cm). Our multi-frequency models allowed us to study the three-dimensional structure of the

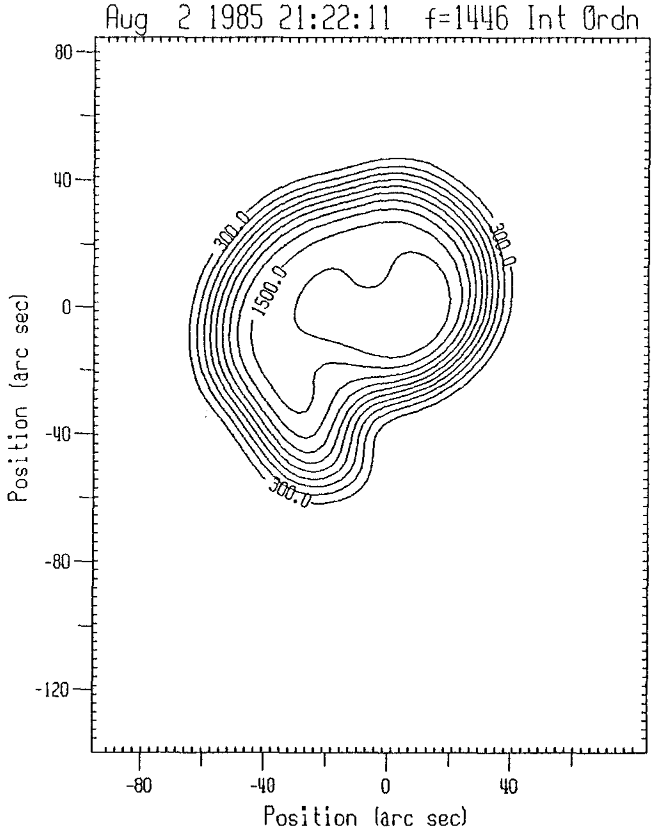

Fig. 9b.

magnetic field above the active region and investigate the relative importance of the gyro-resonance and the free-free emission. The use of pressure measurements in the TR allowed us to relax the plane-parallel assumption and identify microwave structures which were associated with density enhancements. Finally the availability of transverse as well as the longitudinal field measurements permitted us to check the constant α assumption at the photospheric level.

By comparing the observed and the model flux spectra we identified the harmonics responsible for the emission and from those the magnetic field. We estimated field strengths between 1300 G and 1700 G at the base of the TR and between 500 G and 900 G in the low corona above the sunspot. Thus our study provided three independent ways of measuring the magnetic field at different heights in the solar atmosphere. The MSFC and Meudon observations provided direct measurements of the photospheric field while estimates of the magnetic field in the TR and the low corona were obtained from the radio observations. The magnetic field in the corona cannot be measured with confidence from Zeeman splitting of coronal lines; consequently, multi-frequency microwave observations provide a unique tool for

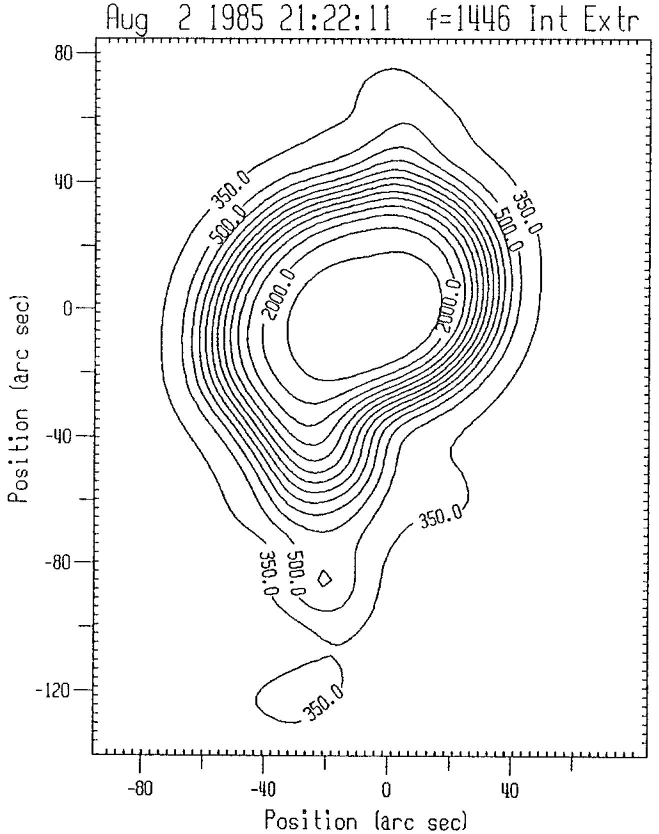

Fig. 9c.

the determination of the three-dimensional structure of the magnetic field in these regions.

In order to fit the radio data to the model, we had to correct the photospheric magnetic field observations. This was probably due to uncertainties in the photospheric observations, which is further supported by the fact that the Meudon observations were not consistent with the MSFC observations (see Sections 2.4 and 3.1). The radio data have a small margin of error and they proved to be a more reliable diagnostic of the magnetic field than the optical observations.

From the comparison of the computed and observed flux spectra we estimated the values of the conductive flux and the height of the base of the TR, whereas we attempted to derive a value of the force-free field parameter, α, from the spatial structure of the VLA maps. The 6 cm maps showed deviations from the current-free model: the peak intensity was not located in the direction of the limb and the low intensity region associated with the location where the magnetic field is almost parallel to the line of sight showed a small eastward displacement with respect of the center of the spot. These deviations were interpreted in terms of non-potential magnetic field.

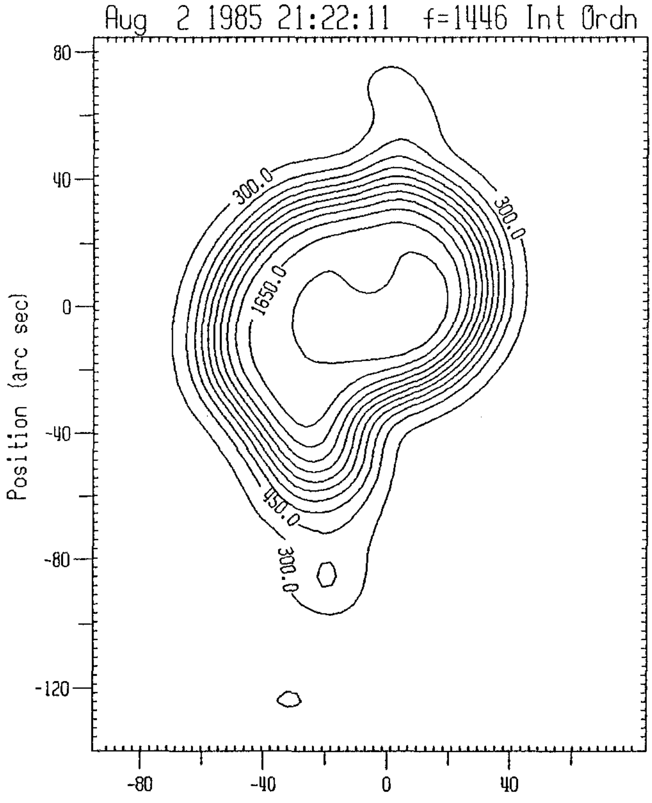

Fig 9d.

Fig. 9a–d. Model computations at 20 cm in R and L circular polarization, for $\alpha = 0$ and for a plane-parallel (a, b) and non-plane-parallel (c, d) pressure model.

We did force-free model computations assuming a constant value of α. However, this may not be a good approximation since α may vary from point to point, remaining constant along the field lines. Indeed, a comparison of the observed and the computed azimuth of the transverse component of the magnetic field showed that the value of α was not constant. It is therefore not surprising that model computations at 6 cm using the same value of α for x-mode and o-mode emission failed to reproduce the structure of the R and L VLA maps. We found that the x-mode emission was better reproduced by a positive-α field and the o-mode emission by a negative-α field.

Our 6 cm computations confirmed the well-known fact that the magnetic field is the principal factor that determines the structure of sunspot associated sources. Indeed, a comparison between the plane-parallel and the non-plane-parallel model maps showed no prominent differences and the free-free contribution to the emission was low. The model maps showed the basic features of gyro-resonance emission from the third and second harmonic. The circular polarization maps

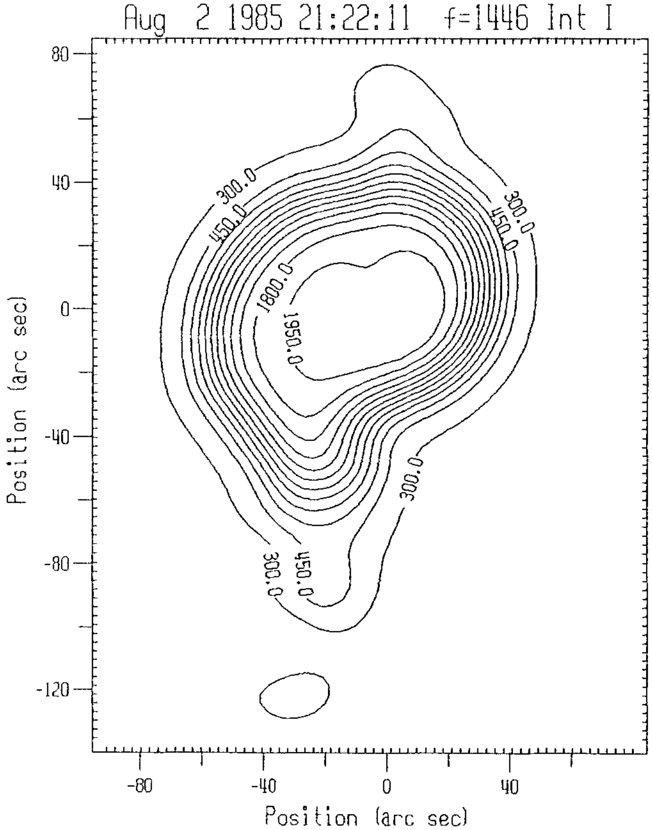

Fig. 10a.

showed three maxima: one was associated with the zero-θ region and the others were located in regions where only the third harmonic was in the corona. The basic difference between the computed and the observed maps at 6 cm was that the region of high T_b was more extended in the model than in the observed map. This may be interpreted in terms of variations of the height of the base of the TR. Other possibilities such as deviations of the magnetic field from the force-free model or deviations from the constant conductive flux assumption should not be excluded.

At 20 cm the emission came from the entire active region; the peak was associated with the sunspot while the diffuse component was associated with the plage. Thus our observations are closer to the view that the large scale 20 cm emission comes primarily from plage regions (Lang, Wilson, and Rayrole, 1982; Dulk and Gary, 1983; Gopalswamy, White, and Kundu, 1991), with a small contribution from coronal loops. Evidence for the latter came from the fact that the diffuse component covered a more extended region in the observed maps than in the model maps.

The differences between plane-parallel and non-plane-parallel model maps was more prominent at 20 than at 6 cm. These differences showed better in the diffuse

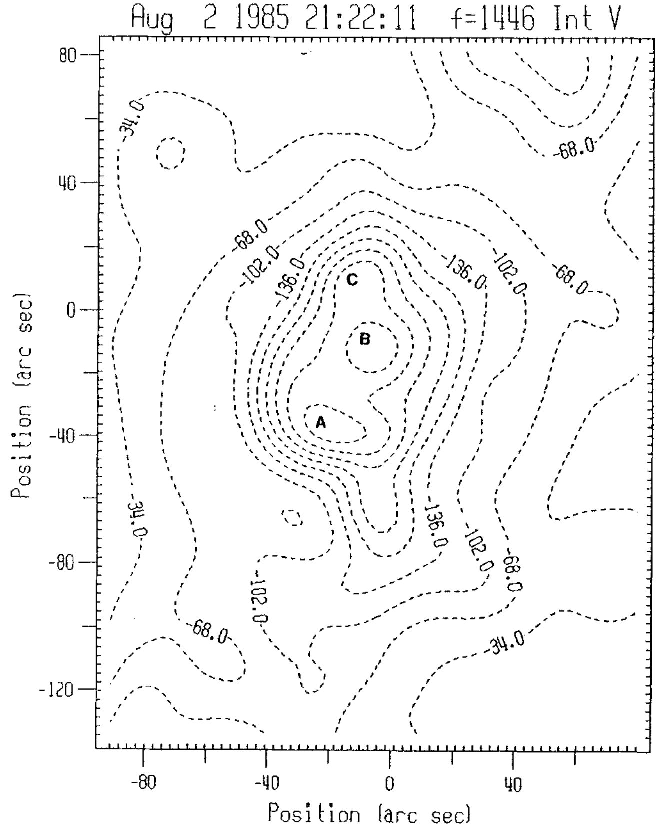

Fig. 10b

Fig. 10a–b. Model I and V maps computed from the non-plane-parallel R and L maps of Figure 9.

component, which was not reproduced well by the plane-parallel models. This verifies the important role of density variations at 20 cm; indeed the average pressure above the plage was a factor of 1.25 higher than the average pressure above the entire active region and a factor of 1.54 higher than the average pressure above the spot. In addition to the free-free emission, there was still some contribution from the gyro-resonance mechanism and this showed better in the V maps. The polarization above the spot was low because both the second and the third harmonics were both located in the corona. Moreover, a polarization maximum was associated with the emergence of the fourth harmonic in the TR in a region where the angle between the field and the line of sight was high.

Acknowledgements

This work has been supported in part through the bilateral exchange agreement between Greece and Russia. This research in the University of Maryland was carried out with support from the National Science Foundation grant ATM-16972 and NASA grant NAG W-1541. The authors wish to thank E. Tandberg-Hansen and B. Schmieder for providing the Marshall and Meudon magnetograms, respectively.

References

Alissandrakis, C. E.: 1981, *Astron. Astrophys.* **100**, 197.
Alissandrakis, C. E. and Kundu, M. R.: 1982, *Astrophys. J.* **253**, L49.
Alissandrakis, C. E., Kundu, M. R., and Lantos, P.: 1980, *Astron. Astrophys.* **82**, 30.
Alissandrakis, C. E., Kundu, M. R., and Shevgaonkar, R. K., 1991, *Astron. Astrophys.* **251**, 276.
Alissandrakis, C. E., Lubyshev, B. I., Smolkov, G. Ya., Krissinel, B. B., Treskov, T. A., Miller, V. G., and Kardapolova, N. N.: 1992, *Solar Phys.* **142**, 341.
Alissandrakis, C. E., Gelfreikh, G. B., Borovik, V. N., Korzhavin, A. N., Nindos, A., and Kundu, M. R.: 1993, *Astron. Astrophys.* **270**, 509.
Dere, K. P., Bartoe, J.-D. F., and Brueckner, G. E.: 1982, *Astrophys. J.* **259**, 366.
Dere, K. P., Schmieder, B., and Alissandrakis, C. E.: 1990, *Astron. Astrophys.* **233**, 207.
Chiuderi-Drago, F., Alissandrakis, C. E., and Hagyard, M.: 1987, *Solar Phys.* **112**, 89.
Dulk, G. A. and Gary, D. E.: 1983, *Astron. Astrophys.* **124**, 103.
Gary, D. E. and Hurford, G. J.: 1987, *Astrophys. J.* **317**, 552.
Gelfreikh, G. B. and Lubyshev, B. I.: 1979, *Astron. Zh.* **56**, 562 (*Soviet Astron.* **23**, 316).
Gopalswamy, N., White, S. M., and Kundu, M. R.: 1991 *Astrophys. J.* **379**, 366.
Kundu, M. R. and Alissandrakis, C. E.: 1984, *Solar Phys.* **94**, 249.
Kundu, M. R., Alissandrakis, C. E., Bregman, J. D., and Hin, A. C.: 1977, *Astrophys. J.* **213**, 278.
Kundu, M. R., Schmahl, E. J., and Fu, Q.-J.: 1989, *Astrophys. J.* **336**, 1078.
Krüger, A., Hildebrandt, J., and Fürstenberg, F.: 1985, *Astron. Astrophys.* **143**, 72.
Lang, K. R., Wilson, R. F., and Rayrole, J.: 1982, *Astrophys. J.* **258**, 384.
McConnel, D. and Kundu, M. R.: 1983, *Astrophys. J.* **269**, 698.
Nindos, A., Alissandrakis, C. E., Gelfreikh, G. B., Borovik, V. N., Korzhavin, A. N., and Bogod, V. M.: 1996, *Solar Phys.* **165**, 41.
Schmieder, B., Raadu, M., Démoulin, P., and Dere, K. P.: 1989, *Astron. Astrophys.* **213**, 402.
Shevgaonkar, R. K. and Kundu, M. R.: 1984, *Astrophys. J.* **283**, 413.
Solnechnye Dannye: 1985, No. 8.
White, S. M., Kundu, M. R., and Gopalswamy, N.: 1991, *Astrophys. J.* **336**, L43.
Zheleznyakov, V. V.: 1970, *Radio Emission of the Sun and Planets*, Pergamon Press, Oxford.